Microstructure evolution of Incoloy 800H in industrial environment and correlation with creep mechanisms from literature

C. Rojas-Ulloa[*1], H. Morch[1], V. Tuninetti[2], J. Tchoufang Tchuindjang[3], O. Pensis[4], A. Di Giovanni[4], A. Mertens[3], L. Duchêne[1], A.M. Habraken[1,5]

[1] ArGEnCo Department, MS2F sector, MSM team, University of Liège, Quartier Polytech 1, allée de la Découverte 9 (B52), 4000 Liège, Belgium
[2] Department of Mechanical Engineering, Universidad de La Frontera, Francisco Salazar 01145, Temuco 4780000, Chile
[3] Department of Aerospace and Mechanical Engineering, MMS team, University of Liège, Quartier Polytech 1, Allée de la Découverte 9 (B52), B-4000 Liège, Belgium
[4] Drever International S.A., 15 Allée des Noisetiers, Liège Science Park, 4000 Liège, Belgium.
[5] Fonds de la Recherche Scientifique −F.R.S.−F.N.R.S. Belgium, 5 rue d'Egmont 1000 Bruxelles, Belgium
ce.rojasulloa@uliege.be

Summary
The microstructures of 800H samples affected by natural corrosion within industrial-like environmental conditions have been studied, and their potential effects on the creep response have been investigated based on literature information. Smooth cylindrical specimens of the alloy extracted from rolled sheet material have been placed into an industrial furnace, where they were exposed to high temperature thermal cycles within an air atmosphere. Samples spending 0 to 5 years inside the furnace underwent a microstructural characterization campaign. Optical microscopy images reveal no grain coarsening. Macroscopic Vickers hardness shows a relatively wide surface hardness range (115≲HV10≲140). Compared to as-received material, micro-hardness profiles from specimens after years of high-temperature exposure exhibit a surface hardening trend within the vicinity of the edge exposed to the environment. Scanning electron microscopy analyses revealed two coexisting corrosion mechanisms: oxidation and nitridation. The latter is identified as the cause of the micro-indentation hardening trend.

Keywords
Austenitic Ni-based alloy, Nitridation, Oxidation, Creep micromechanics, non-classical creep, two-step creep minima

Introduction

Alloy 800H (UNS N08810) is an austenitic Fe-Ni-Cr alloy. It differs from its predecessor alloy 800 by having a specific C content within 0.05 and 0.10% (wt%) and a higher solution annealing (SA) temperature at 1150°C followed by water quenching (WQ) [1]. It combines a good creep and an excellent oxidation and carburization resistance while maintaining a relatively low Ni content compared to similar austenitic alloys. Its good mechanical properties and high-cost efficiency have made of 800H an attractive alloy for high temperature industrial applications, seeing extensive use in metallurgic, petrochemical, and power generation sectors.

Multiple studies seeking to characterize the mechanical response of 800H alloy were conducted in the decades following its development. These entailed extensive experimental campaigns addressing hot tensile [2,3], creep [4–6], and creep-fatigue [7,8] tests. Embedded within the industrial application context, testing temperatures would not surpass the 850°C barrier. Creep curves obtained under such conditions showed a classical creep behaviour, where the standard primary (I), secondary (II) and tertiary (III) creep stages are clearly identified. This classical creep behaviour is represented in Figure 1a. Studies addressing its creep and creep-fatigue response under a variety of multioxidant environments [9,10] evidenced the suitability of the alloy for applications under such conditions. Overall, these pioneering findings led to the approval of the use of 800H alloy for critical components in high temperature gas-cooled reactors [11] according to ASME Section III Code Case 1342 (currently ASME III-NH [12]). In this line, contemporaneous studies inquiring on the possibility of enabling Incoloy 800H to form part of very-high temperature gas-cooled reactors in 4th generation nuclear power plants [11,13,14] or as part of pigtail lines in petrochemical industry [15,16] (where certain variants of the Incoloy 800 family are also used [17,18]) demonstrate the still rampant industrial interest on the subject.

Studies addressing higher temperatures and/or more aggressive thermomechanical loadings were subsequently conducted, seeking to ascertain the 800H mechanical response to meet the new requirements from the development of highly efficient industrial processes and technologies [11,13]. Creep curves obtained from tests venturing into temperatures up to 1000°C and stresses below 50 MPa (see Figure 1b, c) seemed to diverge from classical (Norton-type) creep responses, where conventional creep stages I, II and III are clearly identified (see Figure 1a). This was firstly studied by V. Guttmann & R. Bürgel [19] after conducting creep experiments in air atmosphere where temperatures up to 1000°C and stress down to 11 MPa were considered. Within these thermomechanical loadings, the creep behaviour of 800H is characterized by three non-classical creep stages. They are hereafter referred to as stages A, B, and C in Figure 1b and c.

- Stage A characterizes by a continuous decrement of the creep strain rate ($\dot{p}$) as the creep strain (p) increases. The $\dot{p} - p$ curve follows a hardening trend until a minimum creep strain rate (mcsr) is reached (see Figure 1b and c).
- Stage B starts with an increment in $\dot{p}$ after the mcsr is reached. Thereafter, the $\dot{p} - p$ curve exhibits a damped softening where no stagnation (i.e., steady state $\dot{p}$) is necessarily observed. In the presence of short-term creep tests where the time-to-rupture is roughly found below 600 hours ($t_r \lesssim 600$ h), the behaviour corresponds to the one shown in Figure 1b, where the incremental trend of $\dot{p}$ is held (i.e., $d\dot{p}/dp > 0$). In contrast, in cases where $t_r \gtrsim 600$ h, a secondary creep strain hardening is observed during stage B in the form of a decrement of $\dot{p}$ (i.e., $d\dot{p}/dp < 0$, see Figure 1c). Scanning Electron Microscopy (SEM) images acquired from 800H specimens exhibiting such a creep behaviour show a substantial precipitation of Cr and Al nitrides. This led authors from [19] to firstly associate this creep hardening phenomenon to the nitridation of the material. Nitridation in this alloy has been observed under studies addressing similar conditions [15,20–22]. The creep-hardening effect of nitridation in 800H has been comprehensively studied by A.M. Young et al. [23].
- Stage C is the final creep stage, and is characterized by an increment of $\dot{p}$ following a softening trend. This is attributed to the loss of load-carrying capacity of the material as the internal damage increases up until rupture occurs.

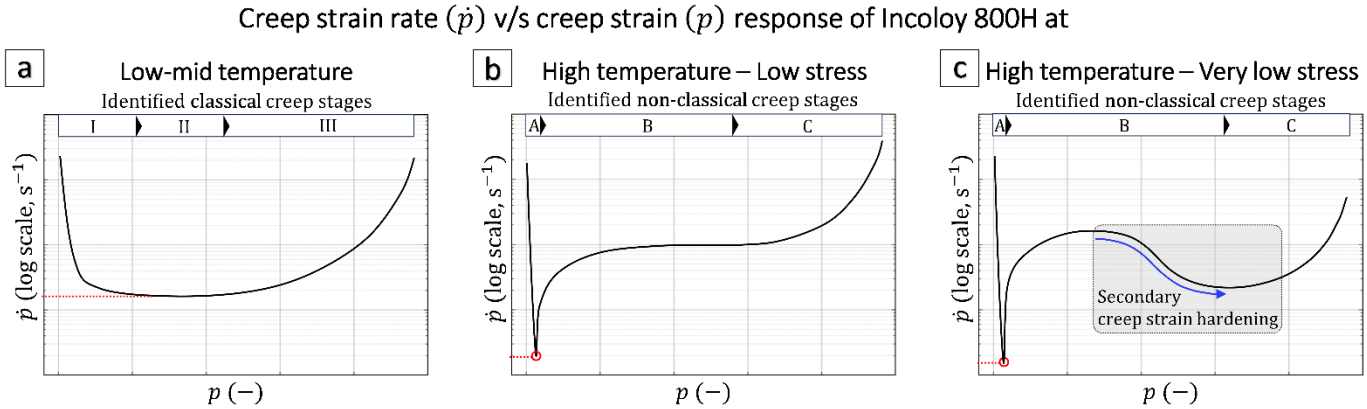

Figure 1 Creep strain rate v/s creep strain curves describing the different viscoplastic responses exhibited by Incoloy 800H under (a) low-mid temperatures, (b) high temperature & low stress, and (c) high-temperature very low stress in air-like atmospheric conditions. In each case, a red line highlights the location of the minimum creep rate.

Similar non-classical creep responses have been reported in other materials, such as 2¼Cr-1Mo [6,24], stainless steel 304 & 316 [6,25], polycrystalline cast copper, Inconel 617, and Ni-superalloys. Despite the similarities, the underlying physical phenomena inducing this creep response may differ. For instance, the non-classical behaviour observed in Ni-based superalloys is attributed to the complex interaction occurring between dislocations and the characteristic γ-γ' phases [26–30]. For Inconel 617, it is attributed to microstructural changes (namely the precipitation of γ' phases and grain twinning) occurring during high-temperature exposure [31,32]. For cast copper, authors attribute the phenomenon to the onset of a transitional creep mechanism, going from a diffusional-driven creep towards a dislocation-driven creep [33,34].

In metals, viscoplastic deformations are attributed to the movement of dislocations, atoms and vacancies found embedded within its crystallographic structure. The specific mechanisms that favour the movement of these crystallographic instabilities are known as creep mechanisms. While some authors have proposed the existence of more mechanisms [35], four main creep mechanisms are widely recognized [36–41]: Low-Temperature creep (LTc), High Temperature creep (HTc), Coble creep (Cc) and Nabarro-Herring creep (NHc). The first two correspond to dislocation-driven creep mechanisms, where the movement of dislocations is produced by the interaction between dislocations as they emit or receive vacancies. During LTc, the movement of dislocations is constrained to their respective slip planes (dislocation sliding), whereas in HTc, dislocations are capable of moving towards other slip planes (dislocation climb). The latter two mechanisms correspond to diffusion-driven creep mechanisms, and are produced by the diffusional movement of vacancies. During Cc, the movement of vacancies is constrained to the grain boundaries, whereas for NHc the diffusion takes place within the crystal lattice. Illustrations describing these four main creep mechanisms and their classification within a generic Ashby map is presented in Figure 2.

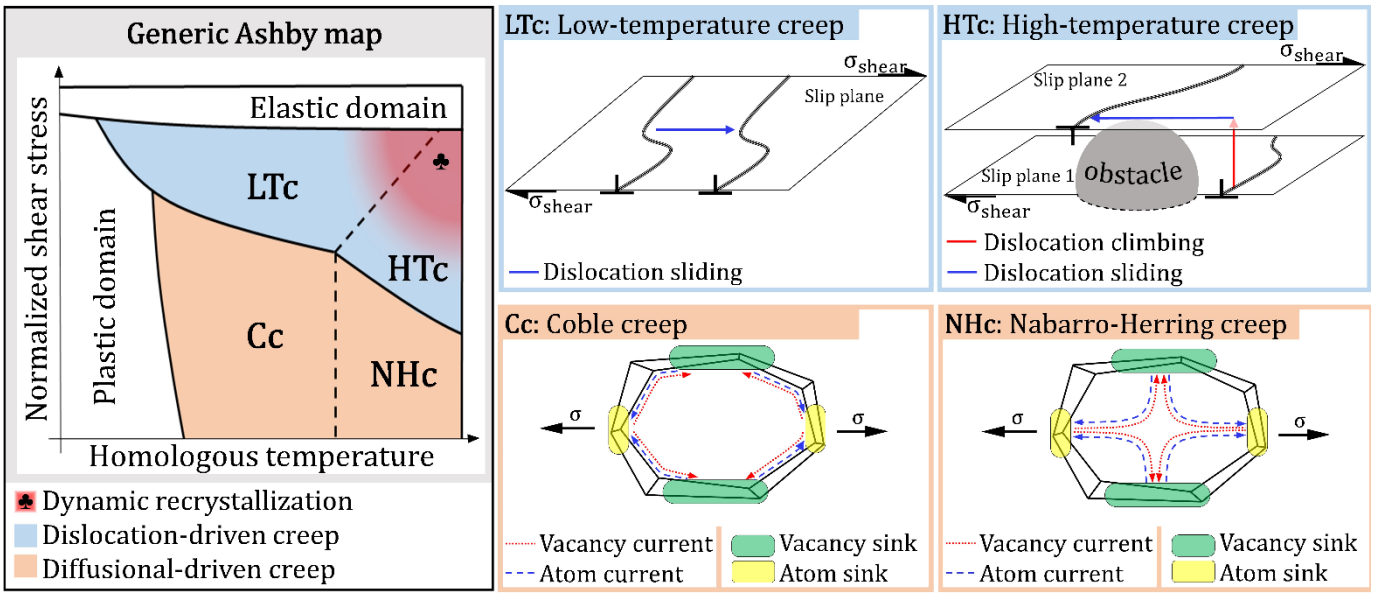

Figure 2 Illustrations describing the physics of low-temperature creep (LTc), high-temperature creep (HTc), Coble creep (Cc) and Nabarro-Herring creep (NHc), and their correspondent location into a generic Ashby map.

From a micromechanical perspective, the good creep resistance of Incoloy 800H is attributed to its relatively large average grain size (AGS) of ASTM Gr. 1-5, its FCC austenitic phase, and its solid-solution state. This last fact entails that during viscoplastic deformations, the dissolved atoms embedded within the crystallographic structure of the material act as obstacles for the movement of dislocations. The continuous pinning and unpinning of dislocations taking place during elevated temperature tensile [42,43] or fatigue [44–46] tests lead to the onset of a dynamic strain aging (DSA) regime. During creep deformations however, the dissolved atoms inhibit the movement of dislocations throughout the crystal lattice, resulting in a higher activation energy for dislocation creep to occur and a subsequent lower $\dot{p}$ [19,41,47]. Studies inquiring on the correlation between microstructural features of 800H and its creep response were performed in [19,21,22], where Transmission Electron Microscope (TEM) images were acquired from samples after undergoing a variety of non-destructive creep tests. In particular, those observations acquired from samples exhibiting classical creep regimes evidence the formation of sub-grain structures in the form of dislocation pile-ups. This was not observed in samples submitted to very high temperatures and low-stress creep tests, where dislocations seem to pile up predominantly at the GBs. The authors from [19] state that the non-classical creep behaviour of 800H is attributed to a creep mechanism transition: stage A exhibits a diffusional-driven creep and stages B and C exhibit a dislocation-driven creep (see Figure 1b), whereas the secondary creep strain hardening shown in Figure 1c is attributed to nitridation. This theory has been widely accepted, and has influenced some recent developments on the subject. For instance, a thorough study on the correlation of the analytical creep response of 800H alloy and its microstructural features (namely grain boundary coherency and AGS) is provided by B. Gardiner's PhD. thesis [15]. In a similar manner, A.M. Young et al. have studied the kinetics of carbides [48] and nitrides [49] in 800H alloy within a controlled environment, and have recently studied the effect of these precipitates on the creep deformation response of the alloy at very high temperatures [23].

Attempts to model the creep response of 800H addressing its non-classical behaviour have reached mild success. For instance, A.L. Beardsley et al. [50] used a genetic algorithm to identify the optimal set of parameters of an analytical Arrhenius-type micromechanics creep model describing the creep behaviour of 800H as the summation of the contributions of the four creep mechanisms described in Figure 2. Following a numerical approach, C. Rojas-Ulloa et al. [51] implemented a modified Graham-Walles viscoplastic function within a Chaboche-type finite element (FE) model to allow the prediction of complex creep responses. Addressing 800H creep data found in literature [19,20], it demonstrated good accuracy in the prediction of creep curves of the type presented in Figure 1b and c. Overall, these attempts highlight the importance of ascertaining the microstructure evolution of Incoloy 800H under high-temperatures as a means to further understand its non-classical creep response.

Material

A single rolled sheet of 800H of dimensions 800×400×18 mm^3 was acquired for this study. The standard chemical composition of the alloy is provided in Table 1. No specific information on the hot rolling process or time spent under SA+WQ process was provided.

Table 1: Standard chemical composition of alloy 800H, after [1].

Element	Ni	Cr	C	Si	Mn	P	S	Ti	Al	Co	Cu	N	Fe
min. wt%	30.0	19.0	0.05	-	-	-	-	0.25	0.25	-	-	-	Bal.
max. wt%	34.0	22.0	0.10	0.70	1.50	0.015	0.010	0.65	0.65	0.50	0.50	0.03	Bal.

Smooth cylindrical specimens of 10 mm diameter were extracted from the sheet. These were placed in an industrial furnace, where they were exposed to a combination of realistic low- and high-frequency thermal cycles reaching up to 1000°C in air at sea-level atmospheric pressure.

To analyse the microstructural changes occurring in the material, specimens have been retrieved from the furnace on a yearly basis. At the time of writing this article, a total of 5 batches of specimens (1 per year) have been recovered from the furnace. These are henceforth identified as N1, N2, N3, N4 and N5, where the number indicates the year of recovery. Samples of as-received material are identified as N0.

Methods

The microstructural evolution of the specimens across years in-furnace was ascertained by conducting a thorough microstructural campaign. This entailed the characterization of microstructural features such as average grain size (AGS), material hardness and material homogeneity across all samples. Methods such as Optical Microscopy (OM), macro-Vickers (MV) indentation, micro-Vickers (μV) indentation, and SEM using Energy-Dispersive X-ray (EDX) sensors were applied.

Microstructural characterization tests were conducted on 6 randomly selected specimens (N0 to N5). One longitudinal (L) and one transversal (T) section were obtained from each smooth bar specimen. These were mounted in bakelite moulds as seen in Figure 3a. The microstructural characterization techniques (OM, MV, μV, and SEM/EDX) were subsequently conducted following the flowchart provided in Figure 3b.

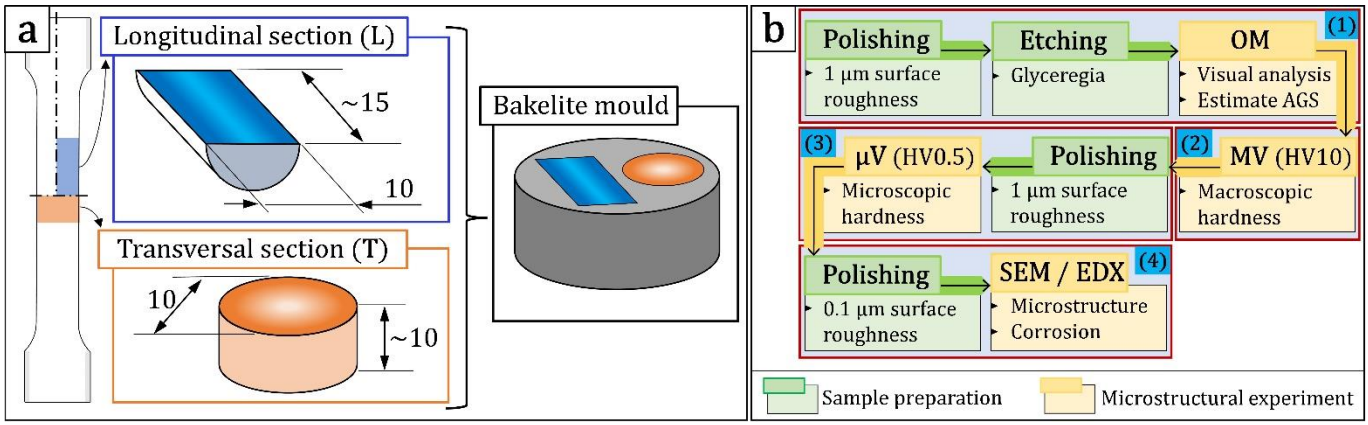

Figure 3 (a) Illustration of the cutting of 800H alloy specimens and mounting into bakelite moulds. (b) Flowchart describing the microstructural characterization campaign conducted per each in-bakelite specimen.

A brief description of the microstructural characterization techniques indicated in Figure 3b addressing their respective metallographic preparation procedures is provided below:

(1) Prior to the OM image acquisition procedure, the surfaces of the samples were grinded with SiC paper and polished down to 1 μm using a polycrystalline diamond suspension. To highlight the GBs, these were etched using glyceregia [15,52]. OM images were then acquired using an Olympus BX60M microscope. The microscope and image acquisition system were electronically controlled using the software Stream Motion. It enables the acquisition of high-quality overview images throughout a surface mapping function, where individually captured images are automatically assembled.

(2) MV hardness measurements were performed on a Universal EMCO M1C 010 hardness testing machine. It was configured to perform 10 kg force-controlled indentations using a Vickers tip (HV10).

(3) To capture possible mechanical effects of corrosion penetrating into the microstructure, the material homogeneity was mapped across the transversal section via micro-indentation. To this end, the samples underwent a new polishing procedure seeking to reach a surface roughness 1 µm. The µV indentation tests consisted in a series of 0.5 kg force-controlled indentations (HV0.5), performed on the same Enco Test hardness testing machine.

(4) After a new polishing procedure where a surface roughness of 0.1 µm was reached, SEM images were taken using a Tescan-Clara device with an accelerating voltage of 15 kV. EDX profiles were obtained using a 10 mm² Bruker SDD detector, which helps achieving a semi-quantitative analysis of the precipitates within the zones of interest.

Results

Optical microscopy

The OM procedure started by the acquisition of an overview image for each Bakelite mould. This image was used for both guiding the acquisition of further detailed OM images of each sample as well as for calculating the AGS. The latter was performed by means of applying the linear intercept method. The line pattern used according to E112-13 [53] is shown in Figure 4a. The AGS measured for each N-specimen is graphically given in Figure 4b. The AGS of the material across all years in-furnace is found within the range ASTM Gr. 2.5, corresponding to approximately 150 µm. The negligible variation of the mean AGS across all specimens indicates the absence of grain coarsening.

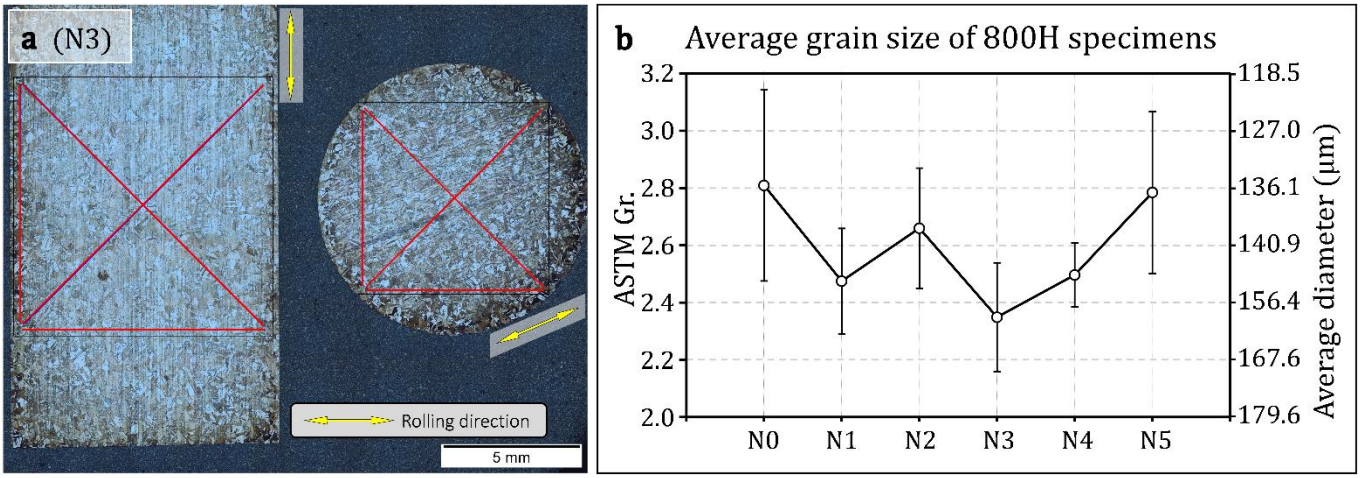

Figure 4 (a) Overview OM image of in-bakelite mould of specimen N3; the red lines are used for calculating the AGS of the alloy via the linear interception method. (b) Graphical depiction of the measured AGS per each N-batch specimen addressing both ASTM Gr. and the equivalent average grain diameter (µm).

Macroscopic surface hardness

To measure the macroscopic Vickers surface hardness, a total of 5 MV indentations per specimen section (L and T) were performed. These were distributed in a cross-like pattern as seen in Figure 5a. The macroscopic hardening analysis, conducted separately for each specimen section, is graphically presented in Figure 5b.

The MV surface hardness of the material was found within the range of 115≲HV10≲140. The hardness differences between both sections L and T are deemed as negligible.

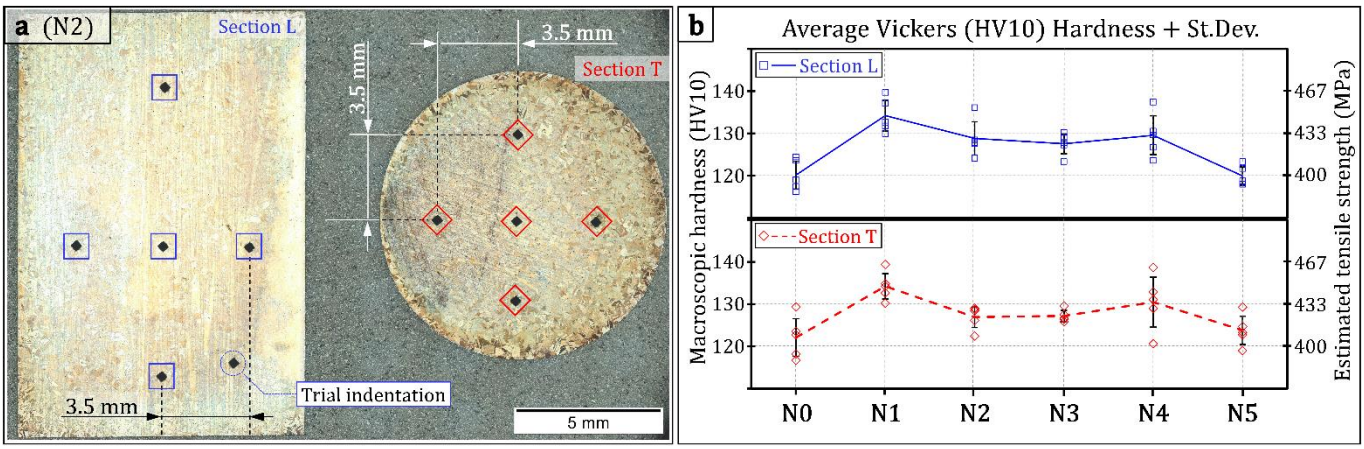

Figure 5 (a) OM image showing the spatial distribution of MV indentations for N2 specimen. (b) HV10 Vickers hardness and estimated tensile strength of as-received and heat-affected specimens of Incoloy 800H.

Microscopic surface hardness

The micro-hardness of the L section of each in-bakelite specimen (see Figure 3a) was mapped across the radial direction of the originally cylindrical specimen ($\vec{r}$ in Figure 6a). To this end, sets of 5 μV indentations (HV0.5) were performed at 13 different location depths. An in-situ example of the resulting 5×13 micro-indentation array is presented for specimen N0 in Figure 6a. This choice encompasses location depths all the way from near-edge edge up until the centre of the sample is reached. The resultant micro-hardness mapping is presented for each specimen in Figure 6b.

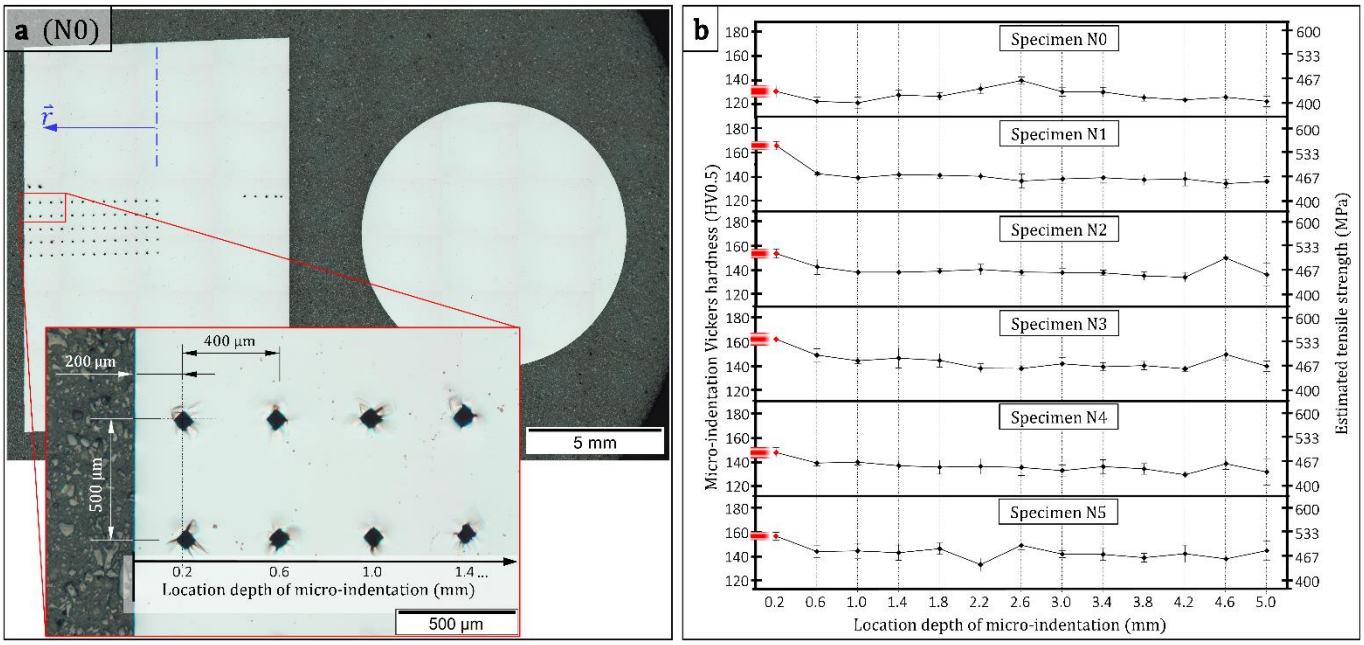

Figure 6 a) Spatial distribution of micro-Vickers hardness measurements. The blue arrow indicates the radial direction from the core of the originally cylindrical specimen. b) Micro-indentation Vickers hardness (HV0.5) and estimated tensile strength of as-received and nitrided samples of Incoloy 800H.

The Vickers hardness magnitude (HV0.5) presented in Figure 6b is found within $120 \lesssim HV0.5 \lesssim 170$, with an average of approximately 140. Compared to specimen N0, the surface hardness of the μV indentation located in the vicinity of the specimen edge (0.2 mm location depth) appears to be higher in all heat-affected specimens (N1 to N5). This is highlighted in red in Figure 6b.

SEM - EDX

The objective of this analysis was to identify key microstructural features in as-received and heat-affected specimens, seeking to correlate the microstructure evolution with the corresponding long-term high-temperature exposure within

an industrial environment. The kinetics of primary (namely $Ti_x(C,N)$, MC and $M_{23}C_6$) and secondary (corrosion related) precipitates is the target. To better understand the behaviour of the latter and their homogeneity across the radial direction of the specimens, the analyses were conducted on section T of each in-bakelite specimen (see Figure 3a). To this end, each T section was subdivided into 5 zones of interest: 1 core (C) and 4 equispaced edge zones (E1 to E4); the location of these zones and their identification is illustrated in Figure 7a.
To identify the alloying elements of the precipitates, their density level from backscattered electron (BSE) images (i.e., gray-scale colour) was contrasted with the corresponding semi-quantitative chemical profiles obtained via EDX. This methodology has been applied with success for the identification of oxides [54] and nitrides [49] in 800H. An example of such an analysis conducted on section E4 of the T section of specimen N5 is provided in Figure 7b.

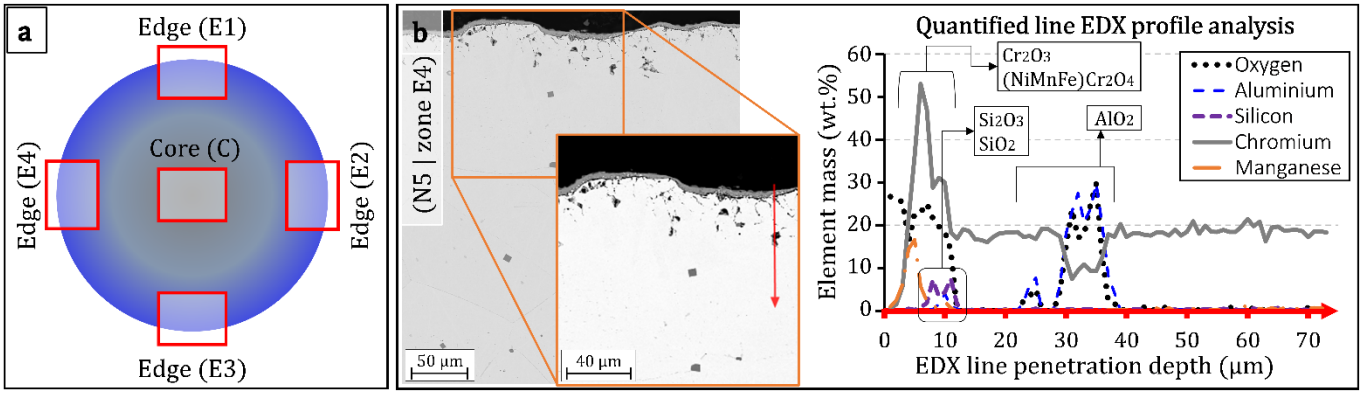

Figure 7 (a) Illustration of the spatial distribution and nomenclature of zones of interest within section T for conducting SEM-EDX analyses. (b) Identification of oxidation-related precipitates in zone E4 of specimen N5 throughout a line EDX profile analysis.

The analysis of the core material (C in Figure 7a) allows the assessment of the microstructure evolution where primary precipitates are exclusively involved (i.e., no corrosion). An overview of this analysis is provided for specimens N0, N1, N3, and N5 in Figure 8a, b, c, and d respectively. Results reveal a progressive dissolution of the carbides of the type MC and $M_{23}C_6$, found initially embedded within the intragranular material microstructure. This phenomenon is accompanied by a consistent intergranular precipitation of chromium-rich carbides. Specimens belonging to years 3 and 5 present an abundant GB precipitation of carbides within the core material.

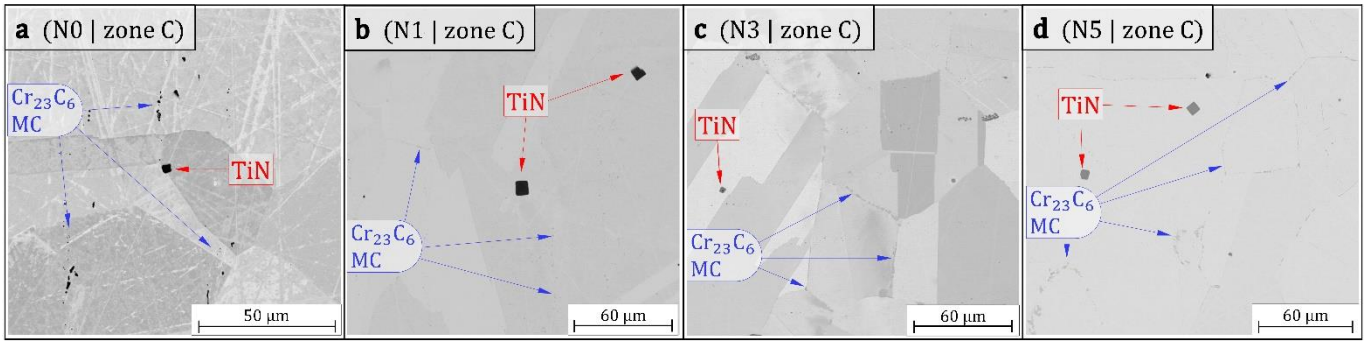

Figure 8 BSE images captured at the core (zone C) of specimens N0 (a), N1 (b), N3 (c) and N5 (d) and identification of primary precipitates.

The edge material (E1 to E4 Figure 7a) was analysed to establish a relation between the industrial environment exposure and the presence of corrosion-related secondary precipitates. The specimen N0 revealed a corrosion-free microstructure, where only the protective thin Cr-rich oxide layer was observed. From N1 to N5 however, two corrosion mechanisms were consistently found: oxidation and nitridation. Nitridation was evidenced by the massive precipitation of bulk and needle-like chromium (CrN and Cr_2N) and aluminium (AlN) nitrides in both intra- and intergranular configurations, as seen for specimen N1 in Figure 9a. Along the years of exposure however, the initially abundant Cr_xN precipitates appear to progressively dissolve into the matrix. This is explained due to the low thermodynamical stability of chromium nitrides [55]. Consequently, reliable observations of nitridation in specimens after long-term exposure is only possible by studying aluminium nitrides, which remain undissolved predominantly

embedded within GBs as seen in Figure 9b related to year 3 (N3). Oxidation was observed in the form of the precipitation of a superficial spinel ((NiMnFe)Cr_2O_4) phases together with Si- and Al- oxides penetrating deeper into the material. The identification of these precipitates in a BSE image acquired from zone E3 from specimen N3 is shown in Figure 9b.

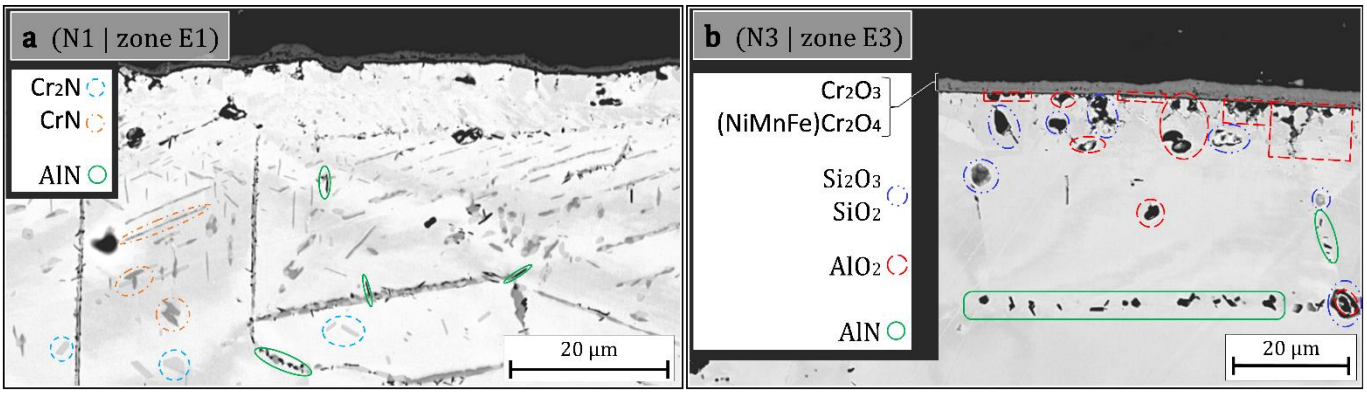

Figure 9 BSE images from edge zones taken from specimens N1 (a) and N3 (b). Due to its higher density, CrN appear darker than Cr_2N in (b); the lightest precipitates such as oxides and AlN in (a) and (b) appear black, and its correct identification is performed with the aid of EDX analyses.

The maximum penetration depth of each corrosion mechanism was measured at the point where the deepest secondary precipitate related to the corrosion mechanism was found. To take into consideration the possible inhomogeneity of the corrosion penetration (i.e., different depth around the specimen), the penetration depth was calculated at the four edge zones (E1 to E4) of the T section as seen in Figure 7a. The maximum penetration of oxidation was entitled to either Al or Si oxides, whereas the maximum nitridation depth is entitled to the presence of AlN. These penetration maximum depths of oxidation and nitridation are graphically presented as function of the years spent in industrial environment in Figure 10a and b, respectively.

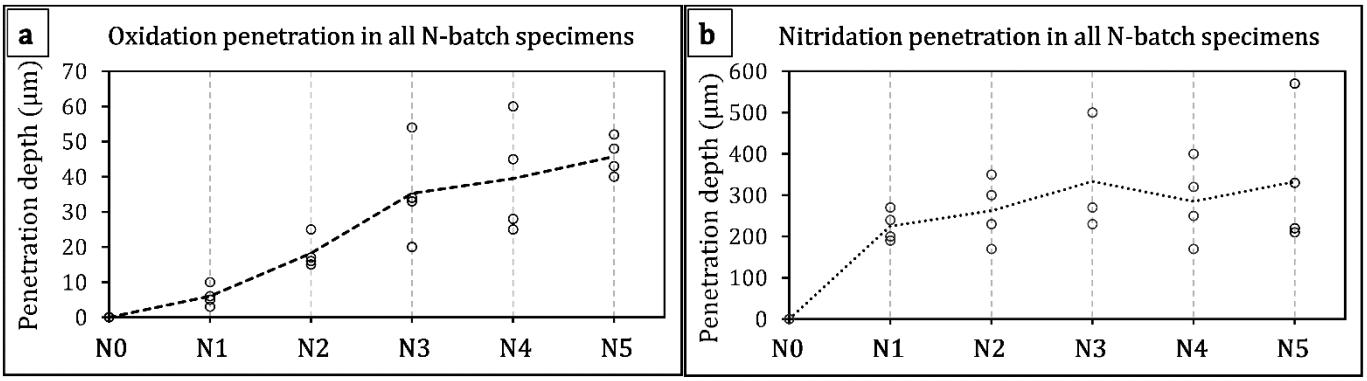

Figure 10 Measured oxidation (a) and nitridation (b) penetration depth into the material based on microstructural observations of the deepest found corrosion-related precipitate. The hollow circular points indicate the maximum depth measured at each edge zone of interest (zones E1 to E4, see Figure 7a).

Contrary to what is observed in controlled nitridation experiments from literature [23,49], the linear interpolation of the average penetration depth of both corrosion mechanisms in Figure 10 does not show a clear parabolic function. Furthermore, the large scattering of the maximum penetration depth data indicates that both corrosion phenomena are not homogeneous. This behaviour is characteristic of corrosion occurring within an industrial operational context: a non-controlled environment where external factors can greatly influence the material behaviour and life span. Finally, the nitridation penetration depth provided in Figure 10b allows to correlate the µV hardness variation detected at 200 µm from the edge of the specimen (see Figure 6b, abscise point 0.2 mm of location depth) to the presence of nitridation-related precipitates.

Discussion

The results presented hereabove evidence that the long-term exposure of Incoloy 800H to high-thermal loadings within an industrial environment is prone to form oxidation and nitridation. The first is widely considered detrimental as it decreases the load carrying capacity of the material, whereas the latter is often overlooked. Besides phenomena such as material sensitization following the precipitation of Cr_xN, nitridation can also lead to a change in the mechanical response of the material. In this research, some of the cylindrical specimens extracted from the furnace were destined to conduct high-temperature creep test. During the experimental procedure, certain components of the creep testing machine experienced failures attributed to the presence of non-uniaxial loadings. The microstructural study presented here was partially motivated by this event, seeking to ascertain the cause of such a failure. Results presented in Figure 10 evidenced that corrosion in the specimens was not homogeneous. According to the experimental studies conducted by A.M. Young et al.[23], the viscoplastic mechanical response of nitrided 800H alloy is characterized by a mcsr of up to 2 orders of magnitude lower than that of aged material. With this assumption, a numerical campaign was initiated. It entailed the execution of finite element (FE) simulations using the FE software Lagamine [56]. The FE model was that of a cylindrical specimen with an inhomogeneous nitrided external layer. Following the quantitative data provided in [23], the viscoplastic behaviour of the core material was that of an aged material, whereas a hardened viscoplastic response was assigned to the inhomogeneous external layer. The numerical results confirmed that the inhomogeneous nitridation of the material induces an inhomogeneous viscoplastic flow. Under the circumstances of creep testing, such a behaviour led to the generation of bending moments which proved detrimental for our creep machine.

The measured microstructure evolution of 800H alloy under a high-temperature industrial environment enables to establish a theoretical relation between its potential creep deformation response and the evolution of key microstructural features. The progressive dissolution of intragranular carbides occurring during the first stages of high-temperature exposure results in a creep strain rate softening as dislocation movement takes place with less particle opposition. This could potentially explain the mcsr softening behaviour of aged 800H alloy observed in [22,23]. An analytical solution to model the creep response of Incoloy 800 addressing carbide dissolution is presented in [3]. Studies of 800H alloy addressing the second creep strain rate minima are yet inconclusive [15,19,20], and a nitridation-induced creep hardening cannot yet be discarded. Microcracks are known to favour the internal nitridation of the alloy [57]. However, it can also be attributed to a grain boundary precipitate strengthening phenomenon induced by the substantial $M_{23}C_6$ grain boundary precipitation exhibited by 800H. Such a behaviour has been reported in similar austenitic Ni-based alloys [58–61]. More studies are needed to ascertain this inquiry.

Conclusions

In this work, the microstructure of 800H specimens exposed to high-temperature industrial environmental conditions was characterized using optical microscopy, macro- and micro-indentation Vickers and Scanning Electron Microscopy coupled with Energy Dispersive X-ray diffraction detector. Under the studied conditions, Incoloy 800H was observed to build two coexisting types of corrosion: oxidation and nitridation. The latter is observed to be the dominant. It was characterized by a massive precipitation of intra- and intergranular CrN, Cr_2N and AlN nitrides diffusing inwards from within the external surface of the specimens. Given the inherent thermodynamical instability of Cr_xN, nitridation in specimens exhibiting more than 4 years of exposure is mainly, if not exclusively, observed in the form of AlN.

The maximum penetration depth of both corrosion mechanisms was determined to be inhomogeneous. This is attributed to a combination of factors inherent of a real industrial environment. The mechanical response of the material exhibiting non-homogeneous nitridation is characterized by the generation of inhomogeneous deformation fields and anisotropic mechanical responses that can be detrimental for certain applications.

With consideration of literature information on creep micromechanics, the evolution of the microstructure studied in this work provides an insight on the influence on the viscoplastic behaviour of the alloy. For instance, the initial dissolution of MC and $M_{23}C_6$ carbides originally found embedded within the crystallographic structure of the material may lead to the loss of the solid-solution characteristics of 800H, thus favouring the unopposed movement of dislocations during creep deformations. Furthermore, the later precipitation of these carbides within GBs can be associated with a grain boundary precipitate strengthening phenomenon, which could potentially explain the second creep strain rate hardening observed in this alloy for very long-term high-temperature creep tests. More studies are needed to ascertain this assumption.

Acknowledgements

Carlos Rojas-Ulloa acknowledges the FNRS for funding this research throughout the FRIA grant N° 4000-8987 and FRIA grant N° 4002-1907. The authors acknowledge the funding from the bilateral research cooperation agreement WBI - Wallonie-Bruxelles/AGCID-Chile 2023-2025 RI-02 (DIE23-0001). As research director of F.R.S.-FNRS, A.M. Habraken thanks the Fund for Scientific Research for financial support.

Declaration of interest statement

The authors declare no conflict of interest.

References

[1] M. Spindler, ECCC data sheet Steel X8NiCrAlTi 32-21 (1.4959, Alloy 800H), (1998).

[2] J.P. Hammond, L.T. Ratcliff, C.R. Brinkman, M.W. Moyer, C.W. Nestor, Jr., Dynamic and Static Measurements of Elastic Constants with Data on 2 1/4 Cr-1 Mo Steel, Types 304 and 316 Stainless Steels, and Alloy 800H, Oak Ridge Laboratory, Oak Ridge, Tennessee, U.S., 1979.

[3] M.E. Abd El-Azim, Correlation between tensile and creep data in alloy 800H at 850°C, Journal of Nuclear Materials 231 (1996) 146–150. https://doi.org/10.1016/0022-3115(96)00352-2.

[4] D.J. Wilson, J.W. Freeman, S.A. Clarence, Creep-Rupture Properties of Sandvik Sanicro 31 Tubing, The University of Michigan, Ann Arbor, Michigan, U.S., 1968.

[5] M.K. Booker, An Analytical Representation of the Creep and Creep-Rupture Behavior of Alloy 800H, Oak Ridge Laboratory, Oak Ridge, Tennessee, U.S., 1978.

[6] M.K. Booker, V.K. Sikka, A Study of Tertiary Creep Instability in Several Elevated-Temperature Structural Materials, Oak Ridge Laboratory, Oak Ridge, Tennessee, U.S., 1978.

[7] H.-J. Penkalla, H. Nickel, F. Schubert, Multiaxial creep of tubes from incoloy 800 H and inconel 617 under static and cyclic loading conditions, Nuclear Engineering and Design 112 (1989) 279–289. https://doi.org/10.1016/0029-5493(89)90163-5.

[8] Z. Mu, K. Bothe, V. Gerold, Damage mechanisms in alloy 800H under creep-fatigue conditions, Fat Frac Eng Mat Struct 17 (1994) 523–537. https://doi.org/10.1111/j.1460-2695.1994.tb00252.x.

[9] P. Soo, R.L. Sabatini, L.G. Epel, J.R.Sr. Hare, High cycle fatigue behavior of Incoloy 800H in a simulated high-temperature gas-cooled reactor helium environment, 1980. https://doi.org/10.2172/5043389.

[10] R.A. Page, J.E. Hack, R.D. Brown, Behavior of Fe-Ni-Cr Alloys in a Complex Multioxidant Environment under Conditions of Dynamic Straining, MTA 15 (1984) 11–22. https://doi.org/10.1007/BF02644382.

[11] R.W. Swindeman, M.J. Swindeman, W. Ren, Can Coverage of Alloy 800H in ASME Section III Subsection NH be Extended to 850°C?, in: Volume 6: Materials and Fabrication, ASMEDC, Vancouver, BC, Canada, 2006: pp. 521–528. https://doi.org/10.1115/PVP2006-ICPVT-11-93333.

[12] Verification of allowable stresses in ASME section III subsection NH for alloy 800H, ASME standards technology, LLC, 2008.

[13] W. Ren, R. Swindeman, Status of Alloy 800 H in Considerations for the Gen IV Nuclear Energy Systems, Journal of Pressure Vessel Technology 136 (2014) 054001. https://doi.org/10.1115/1.4025093.

[14] M. Kolluri, P. ten Pierick, T. Bakker, Characterization of high temperature tensile and creep–fatigue properties of Alloy 800H for intermediate heat exchanger components of (V)HTRs, Nuclear Engineering and Design 284 (2015) 38–49. https://doi.org/10.1016/j.nucengdes.2014.12.017.

[15] B. Gardiner, High temperature creep performance of alloy 800H, PhD. thesis, University of Canterbury, 2014.

[16] S.N. Monteiro, High-Temperature Failure by Perforation of Incoloy 800H Pigtails in Reformer Furnaces, in: K.A. Esaklul (Ed.), Handbook of Case Histories in Failure Analysis, ASM International, 1992: p. 0. https://doi.org/10.31399/asm.fach.v01.c9001108.

[17] R. Dehmolaei, M. Shamanian, A. Kermanpur, Microstructural changes and mechanical properties of Incoloy 800 after 15 years service, Materials Characterization 60 (2009) 246–250. https://doi.org/10.1016/j.matchar.2008.08.012.

[18] L.A. Spyrou, P.I. Sarafoglou, N. Aravas, G.N. Haidemenopoulos, Evaluation of creep damage of INCOLOY 800HT pigtails in a refinery steam reformer unit, Engineering Failure Analysis 45 (2014) 456–469. https://doi.org/10.1016/j.engfailanal.2014.07.017.

[19] V. Guttmann, R. Bürgel, Creep–structural relationship in steel alloy 800 H at 900–1000°C, Metal Science 17 (1983) 549–555. https://doi.org/10.1179/030634583790420475.

[20] K. Tachibana, H. Nishi, M. Eto, Y. Muto, Creep characteristics of Alloy 800H, Japan, 1998. http://inis.iaea.org/search/search.aspx?orig_q=RN:29043501.

[21] H.P. Degischer, H. Aigner, H. Lahodny, K. Spiradek, Qualification of stationary creep of the carbide precipitating alloy 800H, in: High Temperature Alloys, Springer, Dordrecht, 1987: pp. 487–498.

[22] K. Spiradek, H.P. Degischer, H. Lahodny, Correlation between microstructure and the creep behaviour at high temperature of alloy 800 H, in: Materials Science, International Atomic Energy Agency (IAEA), Vienna, Austria, 1989: pp. 54–65.

[23] A.M. Young, M.V. Kral, C.M. Bishop, Effects of aging and nitridation on microstructure and mechanical properties of austenitic stainless steel, J Mater Sci 58 (2023) 10716–10735. https://doi.org/10.1007/s10853-023-08659-1.

[24] R.L. Klueh, R.W. Swindeman, Mechanical properties of a modified 2 1/4 Cr-1 Mo steel for pressure vessel applications, Oak Ridge National Laboratory, 1983.

[25] V.K. Sikka, H.E. McCoy Jr., M.K. Booker, C.R. Brinkman, Heat-to-Heat Variation in Creep Properties of Types 304 and 316 Stainless Steels, Journal of Pressure Vessel Technology 97 (1975) 243–251. https://doi.org/10.1115/1.3454303.

[26] A.K. Singh, N. Louat, K. Sadananda, Dislocation network formation and coherency loss around gamma- prime precipitates in a nickel- base superalloy, MTA 19 (1988) 2965–2973. https://doi.org/10.1007/BF02647723.

[27] T.P. Gabb, S.L. Draper, D.R. Hull, R.A. Mackay, M.V. Nathal, The role of interfacial dislocation networks in high temperature creep of superalloys, Materials Science and Engineering: A 118 (1989) 59–69. https://doi.org/10.1016/0921-5093(89)90058-0.

[28] J.X. Zhang, J.C. Wang, H. Harada, Y. Koizumi, The effect of lattice misfit on the dislocation motion in superalloys during high-temperature low-stress creep, Acta Materialia 53 (2005) 4623–4633. https://doi.org/10.1016/j.actamat.2005.06.013.

[29] L.J. Carroll, Q. Feng, T.M. Pollock, Interfacial Dislocation Networks and Creep in Directional Coarsened Ru-Containing Nickel-Base Single-Crystal Superalloys, Metall and Mat Trans A 39 (2008) 1290–1307. https://doi.org/10.1007/s11661-008-9520-7.

[30] K. Chen, J. Dong, Z. Yao, T. Ni, M. Wang, Creep performance and damage mechanism for Allvac 718Plus superalloy, Materials Science and Engineering: A 738 (2018) 308–322. https://doi.org/10.1016/j.msea.2018.09.088.

[31] J.K. Benz, L.J. Carroll, J.K. Wright, R.N. Wright, T.M. Lillo, Threshold Stress Creep Behavior of Alloy 617 at Intermediate Temperatures, Metall and Mat Trans A 45 (2014) 3010–3022. https://doi.org/10.1007/s11661-014-2244-y.

[32] S. Bagui, M. Mandal, B.K. Sahoo, K. Laha, S. Tarafder, R. Mitra, Investigation of non-classical creep behavior of Inconel 617 alloy at 700 °C and 800 °C through interrupted tests and microstructural characterizations, Materials Science and Engineering: A 832 (2022) 142474. https://doi.org/10.1016/j.msea.2021.142474.

[33] B. Wilshire, A.J. Battenbough, Creep and creep fracture of polycrystalline copper, Materials Science and Engineering: A 443 (2007) 156–166. https://doi.org/10.1016/j.msea.2006.08.094.

[34] D.R. Hayhurst, P.R. Dimmer, M.W. Chernuka, Estimates of the creep rupture lifetime of structures using the finite element method, Journal of the Mechanics and Physics of Solids 23 (1975) 335–350. https://doi.org/10.1016/0022-5096(75)90032-0.

[35] J. Fiala, L. Kloc, J. Čadek, Creep in metals at intermediate temperatures and low stresses: a review, Materials Science and Engineering: A 137 (1991) 163–172. https://doi.org/10.1016/0921-5093(91)90331-G.

[36] S. Dubiez-Le Goff, Comportement et endommagement d'un superalliage élaboré par compression isostatique à chaud, PhD. thesis, École Nationale Supérieure des Mines de Paris, 2003.

[37] J. Röesler, H. Harders, M. Beaker, Mechanical Behaviour of Engineering Materials, Springer, 2007.

[38] H. Oikawa, Y. Iijiyima, Diffusion behaviour of creep-resistant steels, in: Creep-Resistant Steels, Woodhead Publishing Limited, Cambridge, England, 2008: pp. 504–518.

[39] K. Maruyama, Fracture mechanism map and fundamental aspects of creep fracture, in: Creep-Resistant Steels, Woodhead Publishing Limited, Cambridge, England, 2008: pp. 350–364.

[40] T.D. Swinburne, Stochastic Dynamics of Crystal Defects, Springer International Publishing, 2015.

[41] Z. Zhuang, Z. Liu, Y. Cui, Dislocation Mechanism-Based Crystal Plasticity, Elsevier, 2019.

[42] J.K. Wright, L.J. Carroll, C. Cabet, T.M. Lillo, J.K. Benz, J.A. Simpson, W.R. Lloyd, J.A. Chapman, R.N. Wright, Characterization of elevated temperature properties of heat exchanger and steam generator alloys, Nuclear Engineering and Design 251 (2012) 252–260. https://doi.org/10.1016/j.nucengdes.2011.10.034.

[43] A.K. Roy, V. Virupaksha, Performance of alloy 800H for high-temperature heat exchanger applications, Materials Science and Engineering: A 452–453 (2007) 665–672. https://doi.org/10.1016/j.msea.2006.11.082.

[44] K. Bhanu Sankara Rao, H. Schiffers, H. Schuster, G.R. Halford, Temperature and strain-rate effects on low-cycle fatigue behavior of alloy 800H, MMTA 27 (1996) 255–267. https://doi.org/10.1007/BF02648404.

[45] Y. Cao, C. Zhang, C. Zhang, H. Di, G. Huang, Q. Liu, Influence of dynamic strain aging on the mechanical properties and microstructural evolution for Alloy 800H during hot deformation, Materials Science and Engineering: A 724 (2018) 37–44. https://doi.org/10.1016/j.msea.2018.03.074.
[46] K.B.S. Rao, H. Schuster, G.R. Halford, Mechanisms of high-temperature fatigue failure in alloy 800H, MMTA 27 (1996) 851–861. https://doi.org/10.1007/BF02649752.
[47] Z. Huda, Creep Behavior of Materials, in: Mechanical Behavior of Materials, Springer International Publishing, Cham, 2022: pp. 253–265. https://doi.org/10.1007/978-3-030-84927-6_14.
[48] A.M. Young, M.V. Kral, C.M. Bishop, Carbide formation accompanying internal nitridation of austenitic stainless steel, Materials Characterization 184 (2022) 111662. https://doi.org/10.1016/j.matchar.2021.111662.
[49] A.M. Young, M.V. Kral, C.M. Bishop, Time–Temperature–Precipitation Relations for Nitrides and Evaluation of Internal Oxidation Theory for Nitridation of Austenitic Stainless Steel, Metall Mater Trans A 51 (2020) 4456–4470. https://doi.org/10.1007/s11661-020-05868-0.
[50] A.L. Beardsley, C.M. Bishop, M.V. Kral, A Deformation Mechanism Map for Incoloy 800H Optimized Using the Genetic Algorithm, Metall and Mat Trans A 50 (2019) 4098–4110. https://doi.org/10.1007/s11661-019-05350-6.
[51] C. Rojas-Ulloa, H. Morch, V. Tuninetti, L. Duchêne, A.M. Habraken, Implementation of a modified Graham-Walles viscosity function within a Chaboche viscoplastic constitutive model, CAMWA 155 (2024) 165–175. https://doi.org/10.1016/j.camwa.2023.12.002.
[52] D. Drabble, The effect of grain boundary engineering on the properties of incoloy 800H/HT, Thesis, University of Canterbury, 2010. http://hdl.handle.net/10092/6194.
[53] Standard Test Methods for Determining Average Grain Size, ASTM international, 2021.
[54] S. Bsat, X. Huang, Corrosion Behaviour of Alloy 800H in Low Density Superheated Steam, ISIJ International 56 (2016) 1067–1075. https://doi.org/10.2355/isijinternational.ISIJINT-2015-651.
[55] U. Krupp, H.-J. Christ, Selective oxidation and internal nitridation during high-temperature exposure of single-crystalline nickel-base superalloys, Metall Mater Trans A 31 (2000) 47–56. https://doi.org/10.1007/s11661-000-0051-0.
[56] MSM, GEG, Lagamine code, (n.d.). http://www.lagamine.uliege.be/dokuwiki/doku.php/.
[57] M. Welker, A. Rahmel, M. Schütze, Oxidation and nitridation of alloy 800 H at a growing creep crack and for unstressed samples, Metallurgical Transactions A 20 (1989) 1541–1551. https://doi.org/10.1007/BF02665510.
[58] K. Sawada, T. Hatakeyama, K. Sekido, K. Kimura, Microstructural changes and creep-strength degradation in 18Cr-9Ni-3Cu-Nb-N steel, Materials Characterization 178 (2021) 111286. https://doi.org/10.1016/j.matchar.2021.111286.
[59] T. Hatakeyama, K. Sawada, T. Hara, K. Sekido, K. Kimura, Three-dimensional analysis of the precipitation behavior of 18Cr–9Ni–3Cu–Nb–N steel at 973 K, Scripta Materialia 200 (2021) 113904. https://doi.org/10.1016/j.scriptamat.2021.113904.
[60] T. Hatakeyama, K. Sawada, K. Sekido, T. Hara, K. Kimura, Influence of dynamic microstructural changes on the complex creep deformation behavior of 25Cr–20Ni–Nb–N steel at 873 K, Materials Science and Engineering: A 814 (2021) 141270. https://doi.org/10.1016/j.msea.2021.141270.
[61] T. Hatakeyama, K. Sawada, K. Sekido, T. Hara, K. Kimura, Microstructural factors of the complex creep rate change in 18Cr–9Ni–3Cu–Nb–N steel, Materials Science and Engineering: A 831 (2022) 142225. https://doi.org/10.1016/j.msea.2021.142225.